Int. J. Electrochem. Sci., 11 **(2016)** 10763 – 10778, doi: 10.20964/2016.12.89

International Journal of ELECTROCHEMICAL SCIENCE
www.electrochemsci.org

Durability and Activity Tunable Pt/Graphene Catalyst for Oxygen Reduction Reactions

Piao Zhang, Wenmao Tu[*]*, Rui Wang, Shichang Cai, Jing Wu, Qiong Yan, Hongfei Pan, Haining Zhang, Haolin Tang*[*]

State Key Laboratory of Advanced Technology for Materials Synthesis and Processing, Wuhan University of Technology, Wuhan 430070, P. R. China.
[*]E-mail: tuwm@whut.edu.cn, thln@whut.edu.cn

Received: 6 September 2016 / *Accepted:* 24 October 2016 / *Published:* 10 November 2016

We report durability and activity tunable Pt/graphene with micropores controllable graphene as the supports for oxygen reduction reactions. The graphene supports are prepared by thermal reduction of few-layered graphite oxide in hydrogen atmosphere. Oxygen atoms emission and carbon atoms rearrangement occur during the thermal reduction at variable temperature, thus form tunable micropores and graphitization degree in the graphene supports. Symmetrical dispersion of Pt nanoparticles with an medial diameter of 2.3 nm loaded on stable graphene supports contribute to a supernal electrochemical surface area, enhanced electrochemical catalytic activity and durability toward oxygen reduction reactions compared to mercantile Pt/C catalyst. The results demonstrate that durability and activity tunable Pt/graphene is a promising electrocatalyst for oxygen reduction in fuel cells.

Keywords: Durability; Activity tunable; Oxygen reduction reaction; Micropores; Graphene supports.

1. INTRODUCTION

With the consumption of fossil fuels, the contamination of environment has become increasingly serious. Polymer Electrolyte Membrane Fuel Cells (PEMFCs), as new energy storage and switching equipment, then arise at the historic moment. PEMFCs are known as environmental-friendly power sources with high efficiency. Electrocatalyst plays a crucial role in the activity and durability of cell performance [1]. Currently, Pt/C catalyst is still the most widely used electrocatalyst in PEMFCs [2]. However, extreme acidity, high electrode potential, and large oxygen concentration conditions do harmful to the lifetime of Pt/C catalyst. Suffering from electrochemical oxidation, carbon black is instable and preferable to be corroded, while Pt nanoparticles will aggregate or detach from the carbon

supports, resulting in poor activity [3]. To enhance the efficiency and durability of catalyst, much effort has been devoted to obtain the proper supports for PEMFCs, including graphitized carbon nanotubes or nanofiber [4, 5] and graphitic mesoporous carbon [6]. Metal oxides or Pt-alloy can be also used as supports to develop the durability of Pt catalyst [7-9]. Nevertheless, either high cost or low specific surface area remains problematic.

Using carbon with high degree of graphitization is a tactics to restrain carbon supports corrosion [10-12]. Combining with its high specific surface area, outstanding electrical conductivity, superior chemical resistance, and particular graphitized basal plane structure, graphene has attracted much attention to be a promising catalyst supports for PEMFCs [13-15]. Recently, numerous works have been reported on graphene as the catalyst support in PEMFCs [16-20]. However, the mechanism and structure of Pt/graphene catalyst to enhance the activity and durability for oxygen reduction is still unclear.

In this paper, we report the durability and activity tunable Pt/graphene with micropores controllable graphene as the supports for oxygen reduction reactions. A templateless and economic exfoliation method for massive synthesis of graphene is reported. During the thermal reduction at variable temperatures, the emission of oxygen atoms and the rearrangement of carbon atoms result in tunable micropores and graphitization extent in the graphene supports. Thus the as-prepared Pt/graphene catalyst exhibits variant activity and durability towards oxygen reduction reactions.

2. EXPERIMENT

2.1. Materials

Natural Flake Graphite (G), Sodium Nitrate ($NaNO_3$, 99.0%), Potassium Permanganate ($KMnO_4$, 99.5%), Concentrated Sulfuric Acid (H_2SO_4, 98%), Hydrogen Peroxide (H_2O_2, 30%) were purchased from Sinopharm Chemical Reagent Co.Ltd. Deionized Water (18.25MΩcm) was produced by a Millipore System.

2.2. Synthesis of graphite oxide (GO), graphene (Gr) and Pt/Gr

GO was synthesized from natural flake graphite by the well-known modified Hummers method [21, 22]. The loose and porous GO was obtained via the freeze-drying technique. Then the GO sample was placed in an Alumina crucible with controlled atmosphere furnace. Before heating, air in the furnace was removed under vacuum and then Ar was pumped in for one hour to keep an oxygen-free environment. Temperature was subsequently raised to several hundred degrees Celsius under the heating rate of $5℃\cdot min^{-1}$. The mixed gas of hydrogen (5% ppm) and argon was flowed at the specified temperature for 2 h. The desired graphene was thus obtained.

Pt/Gr electrocatalyst was fabricated by reduction method. As a kind of reducing agent, ethylene glycol (EG) was used [6]. Typically, 5.309 mL H_2PtCl_6 solution (3.767 $mg\cdot mL^{-1}$Pt) was added into 60 mL EG solution dropwisely under stirring for 30 min constantly. After using NaOH (1 M) to adjust the

pH of the solution above 12, 80 mg graphene was added, followed by ultrasonic treatment and stirring of the solution for 1 h. In order to ensure the completely reduction of H_2PtCl_6, the obtained solution was kept at 130℃ still for 4 h under reflux. After cooling to ambient temperature, the pH was modulated to below 2 with dilute HNO_3, which contributes to the Pt be fully absorbed [23]. Making sure no Cl^- was founded in the as-prepared catalyst which was cleaned with deionized water and then dried in vacuum. The resulted Pt/Gr catalyst has the Pt content of 20 wt.%.

2.3. Materials characterization

The samples were characterized by field emission scanning electron microscope (SEM) and field emission transmission electron microscopy (TEM) with a Zeiss Ultra Plus SEM and a JEM2100F TEM, respectively. In the range of 500 to 4000cm^{-1} by the KBr pellet technology, the identification and characterization of function groups were measured with Nicolet 6700 Fourier transform infrared spectroscope (FTIR). X-ray diffraction (XRD) was conducted with D8 Adwance. The Raman spectra were recorded by INVIA RENISHAW Raman microscope with 633nm argon ion laser excitation. Brunauer-Emmett-Teller (BET) surface area was determined by recording nitrogen adsorption/ desorption isotherms at 77K. The surface chemical constituents of the samples were analyzed by X-ray photoelectron spectroscopy.

2.4. Electrochemical measurement

The electrochemical tests were conducted with a CHI660A station. Platinum black and Hg/Hg_2Cl_2 were served as the counter electrode and reference electrode, severally. Before each experiment, glassy carbon electrode (GCE) should be clean and polished. To prepare the working electrode, a mixed solution was formed with 5 mg catalyst, 100 μl deionized water, 900 μl isopropanol, 20 μl Nafion (5 wt.%, DuPont Co. Ltd.) and a homogeneous black ink via an ultrasonicator. Then 10 μl of the ink was dropped on GCE and condensed at ambient temperature.

Electrochemical tests were performed on a rotating disc electrode (RDE) with a three-electrode test system. Before testing, the activation of the catalyst was conducted with cyclic voltammetry (CV) scanning in the region of 0~1.2 V with a scan rate of 500 $mV \cdot s^{-1}$ and in 0.1 M $HClO_4$ solution with N_2-purged until a stable CV curve was gained. So as to confirm the electrochemical surface area (ESA), CVs were performed at a precision scan rate of 50 $mV \cdot s^{-1}$. Linear sweep voltammograms (LSVs) were measured in a range of 0.2~1.2V at a scan rate of 5 $mV \cdot s^{-1}$ and a rotate rate of 1600 rpm in 0.1 M HClO4 solution with O_2-saturated for oxygen reduction reaction (ORR).

Durability tests were implemented with potential step method [24] in $HClO_4$ solution (0.1 M), which are crucial to assess the quality of the catalyst. The range of potential between 0~1.2V was picked up to measure the stability of the catalyst. Before and after the degradation test, CVs in 0.1 M $HClO_4$ solution with N_2-purged at a scan rate of 50 $mV \cdot s^{-1}$ and LSVs in 0.1 M $HClO_4$ with O_2-saturated at a scan rate of 5 $mV \cdot s^{-1}$ were recorded.

All tests were done under ambient temperature, and the above potentials were shown versus reversible hydrogen electrode (RHE).

3. RESULTS AND DISCUSSIONS

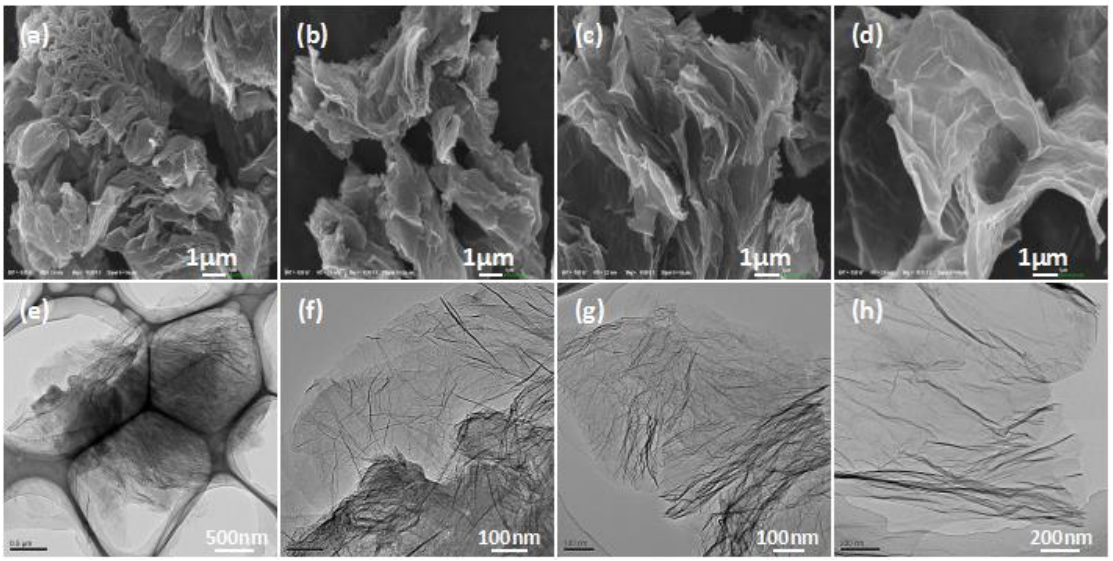

Figure 1. SEM and TEM images of Gr-200 (a, e), Gr-300 (b, f), Gr-400 (c, g), and Gr-500 (d, h), respectively.

Fig. 1 shows the typical SEM and TEM images of graphene sheets at different treating temperatures.

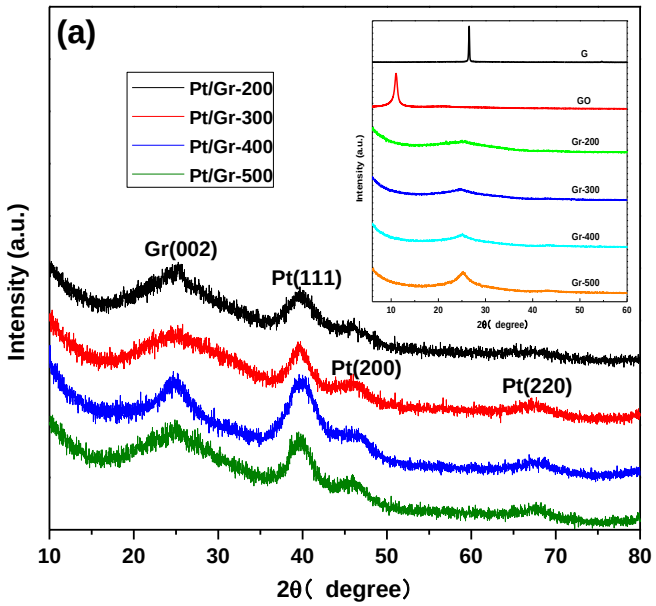

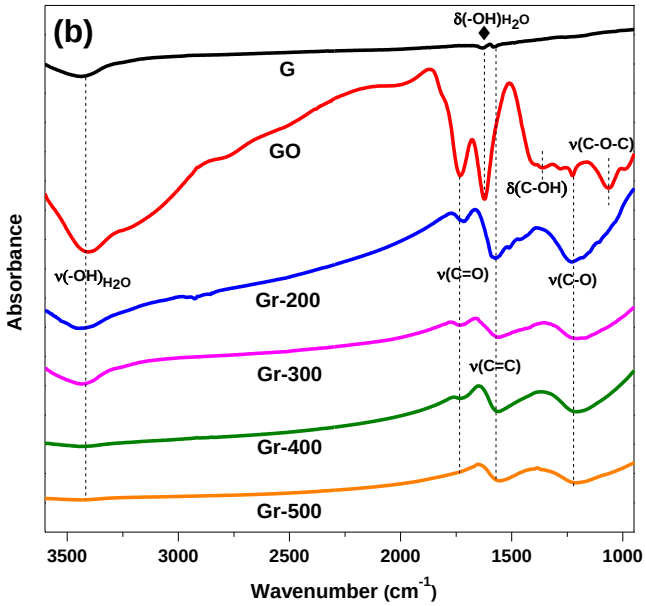

Figure 2. X-ray diffraction patterns and FT-IR spectra of G, GO, Gr and Pt/Gr.

The rapid and efficient wipe off -OH and other oxygen containing groups through thermal reduction result in a folded construction. The ultrathin walls of Gr are almost transparent in comparison to GO under SEM electron irradiation, suggesting that GO sheets were efficiently exfoliated to graphene sheets. Large surface of Gr was yielded by a few layers of graphene sheets with the wrinkled and rippled structure. Moreover, the generated Gr has the same morphology as the three-dimensional graphene, which is featured by fully interconnected porous frameworks [25].The microtopography of Gr was observed by TEM. The lower contrast images of Gr indicate that after thermal reduction the graphene sheets possessed few layers. In addition, with the increase in temperature, the few-layered graphene sheets became more and more filmy and transparent, indicating an increased specific surface area.

The characteristic X-ray diffraction diffractograms of G, GO, Gr and Pt/Gr are showed in Fig. 2a. An intensive crystalline peak (002) of G appears at nearly 26° with a typical interlayer spacing of 0.33 nm, declaring that the graphite is aligned orderly. In GO, the peak of (002) disappeared with the appearance of a high strength diffraction peak arises at 11°, corresponding to graphite oxide (001). Furthermore, the interlayer spacing is calculated to be about 0.77 nm, indicating the intercalation of oxygen containing functional groups. A broad peak of Gr appears at 25° instead of the peak at 11° after exfoliation suggesting a vast removal of oxygen containing functional groups and water from the interlayer and a heavily loss of long range order in graphene during thermal exfoliation. Despite of the peak intensity, the curves of Gr-200, Gr-300, Gr-400 and Gr-500 are very similar. The XRD patterns for the fabricated catalysts of Pt/Gr-200, Pt/Gr-300, Pt/Gr-400 and Pt/Gr-500 uncover the diffraction maximums of graphene and platinum. The C (002) diffraction peak at $2\theta=25°$ for Pt/Gr is similar with the graphene supports. An outstanding crystalline structure of Pt can be proved by the intensive

diffraction maximums at 40.0°, 46.4° and 67.4°, which are corresponding to Pt (111), Pt (200) and Pt (220) are in accordance with the face-centered cubic crystal structure of Pt.

Infrared spectra of G, GO and Gr are presented in Fig. 2b. Absorption band centered at 3434 cm^{-1} of sample G corresponds to the -OH stretching vibration and absorption band at 1634 cm^{-1} refers to the -OH deformation vibration. The absorption band at 1582 cm^{-1} is identified as C=C stretching vibration from sp^2 bonds. In GO, the highly broadened bands at 3407 cm^{-1} and 1623 cm^{-1} relate to the -OH stretching and deformation vibration indicate that GO sample contains a large quantity of adsorbed water. The intense peaks of C=O (1732 cm^{-1}), C-OH (1360 cm^{-1}), C-O (1227 cm^{-1}) and C-O-C (1065 cm^{-1}) suggest that the GO sample is well oxidized and contains mainly -OH and other oxygen containing functional groups.

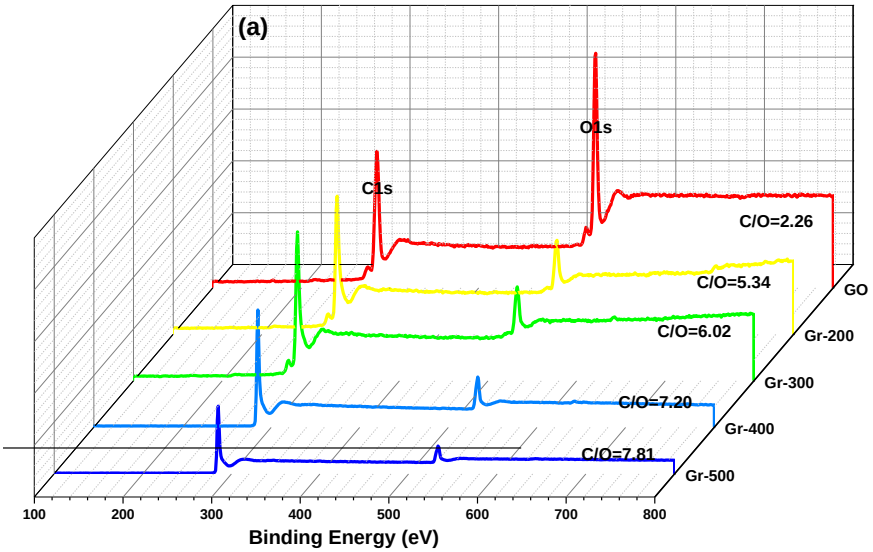

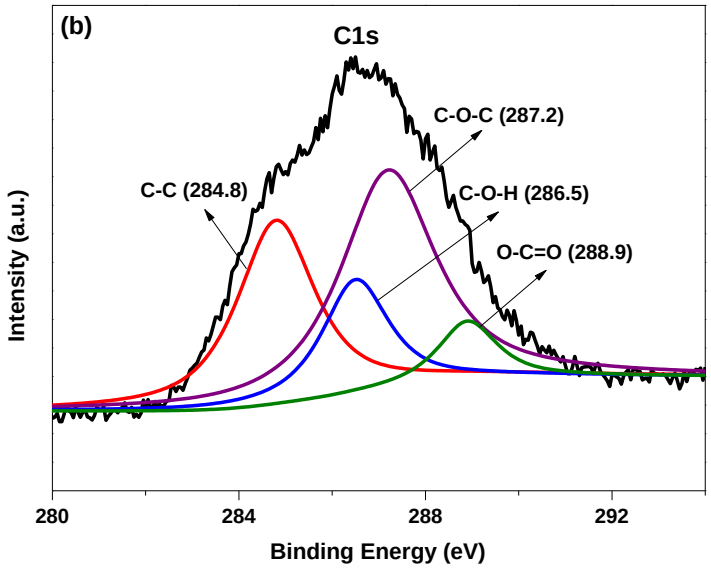

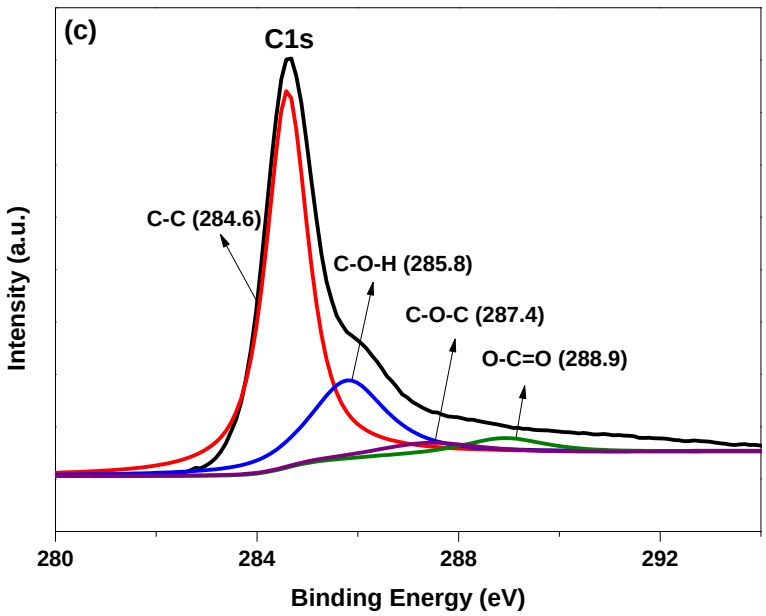

Figure 3. XPS survey spectra of GO and Gr (a); XPS C1s spectra of GO (b) and Gr (c).

Later, -OH (3407 cm^{-1}) is greatly reduced in intensity and -OH (1623 cm^{-1}) disappeared after exfoliation. C=C (1551 cm^{-1}) from sp^2 bonds can be also found in Gr. It is clearly seen that the strength of the peaks at 1732 cm^{-1}, 1360 cm^{-1}, 1227 cm^{-1}, 1065 cm^{-1} referring to C=O, C-OH, C-O and C-O-C are significantly reduced or nearly disappeared after exfoliation indicating the great reduction of these functional groups. By compared with Gr-200, Gr-300, Gr-400 and Gr-500, the -OH (3407 cm^{-1}) and C=O (1732 cm^{-1}) are gradually reduced and even disappeared in Gr-500, indicating that the severe condition is favorable for removal of oxygen-contained functional groups.

The great changes from GO to Gr through thermal reduction can be clearly seen by XPS measurements [26]. The XPS patterns of GO and Gr are shown in Fig. 3, respectively. There are two characteristic peaks at 285 and 533 eV, which correspond to C1s peak and O1s peak respectively presented in XPS survey spectra. With integration of corresponding peaks, one can obtain the ratios of C/O as 2.26 (GO), 5.34 (Gr-200), 6.02 (Gr-300), 7.20 (Gr-400) and 7.81 (Gr-500). The increasing of the ratios from 2.26 to 7.81 indicates the efficient deoxidation of GO. The C1s XPS spectrum of GO exhibits four peaks centered at 284.8, 286.5, 287.2 and 288.9 eV corresponding to C-C, C-OH, C-O-C and O-C=O bonds, respectively [27]. However, after thermal treatment, the peak intensities of the oxygen containing groups decrease obviously. It explains that most of the epoxide and hydroxyl functional groups were reduced during the hydrogen thermal reduction.

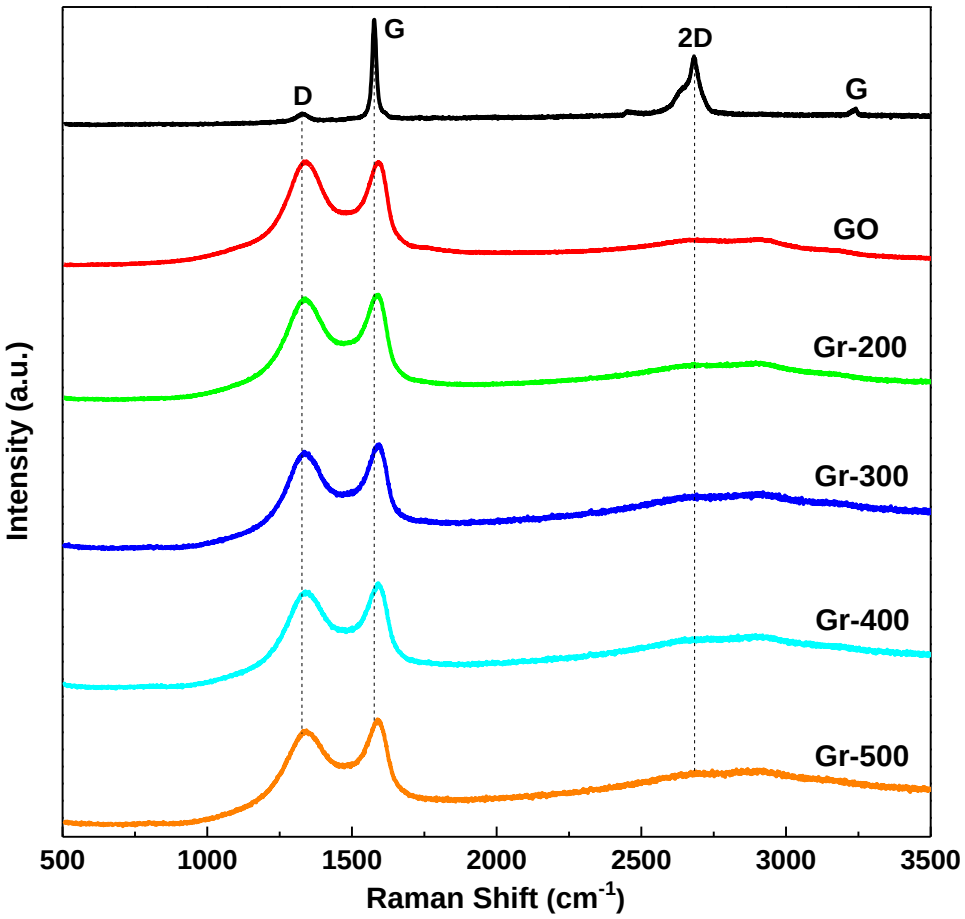

Figure 4. Raman spectra of G, GO and Gr showing different bands.

Raman spectra of G, GO, and Gr are collected, as shown in Fig. 4. The peak located at 1329 cm^{-1} for graphite is assigned to the D-band, which resulted from sp^3 hybridized carbon, suggesting a flawless graphite. A highly intensive G-band occurs at 1577 cm^{-1} allowed E_{2g} phonons at Brillouin zone center [28]. The G-band of GO could be observed at 1592 cm^{-1}, while it transfered back to 1588 cm^{-1}, which closes to the original graphite, revealing the successful reduction of GO after the thermal treatment. Furthermore, a broaden G-band in GO or Gr is attributed to an increase in the disorder. It is known that modified Hummers method and hydrogen thermal exfoliation technology induce defects in the graphitic structure. The ratio of the intensity of D and G bands is adopted to predict the existence of defects and the graphitization degree of catalyst supports. The high I_D/I_G ratio of about 1.0081 for GO reveals the large number of defective sites compared to graphite. A good restoration of π-conjugated structure of graphene can be concluded by the mutative ratios (ranging from 0.9718 to 0.9125). The decreased I_D/I_G ratios reveal an increased graphitization degree of Gr. This is also supported by the shifted wavenumbers of D and G bands (Table 1).

Table 1. The positions of D and G bands in G, GO and Gr. The intensity ratios of these bands are also given.

Sample	D/cm^{-1}	G/cm^{-1}	I_D/I_G
G	1329.37	1557.41	0.1506
GO	1342.67	1591.97	1.0081
Gr-200	1339.67	1591.80	0.9718
Gr-300	1336.85	1591.50	0.9420
Gr-400	1339.67	1591.80	0.9381
Gr-500	1334.97	1588.19	0.9125

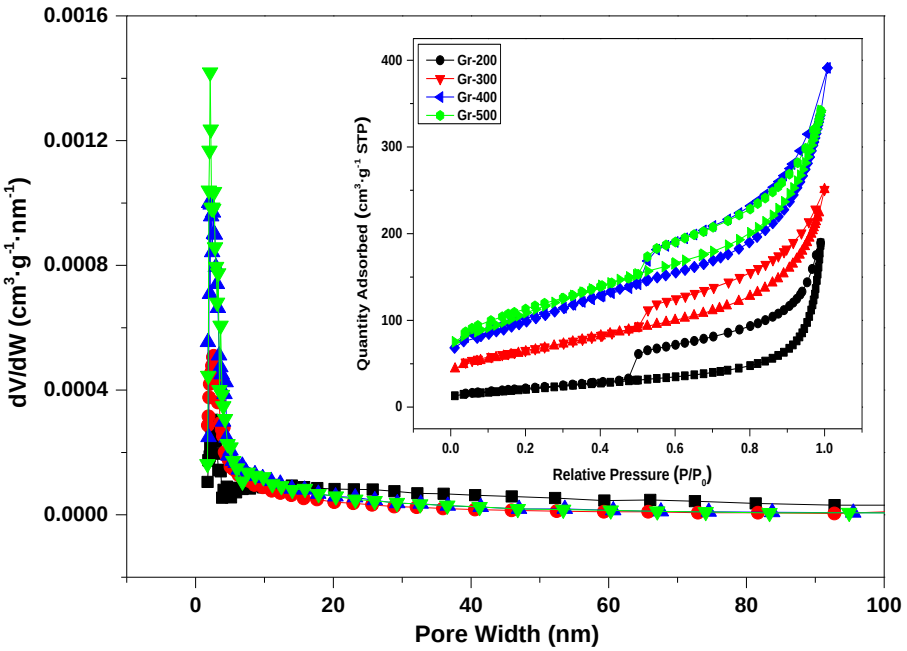

Figure 5. Nitrogen adsorption/ desorption curves for determining BET surface area, and pore size distribution collected for Gr-200, Gr-300, Gr-400 and Gr-500, respectively.

Nitrogen adsorption and desorption isotherms for graphene supports are presented in Fig. 5. Using Brunauer-Emmett-Teller (BET) analysis, a specific surface area of Gr-500 is calculated to be 389.3 m^2/g (194.4 m^2/g for Gr 200, 223.7 m^2/g for Gr-300, and 353.9 m^2/g for Gr-400), which is much larger than that of GO (76.3 m^2/g), demonstrating that the surface area has been greatly increased by hydrogen thermal reduction process. After exfoliation, a mass of micropores formed by the emission of oxygen atoms. From the pore size distribution diagram, one can clearly see the existence of micropores which are beneficial for loading Pt nanoparticles on graphene supports. Due to the harsher and more demanding condition, the micropores and specific surface area of graphene increased with the rise of temperature. The mesoporous can be also seen from the diagram, which may be caused by the irregular stack of few-layered graphene sheets

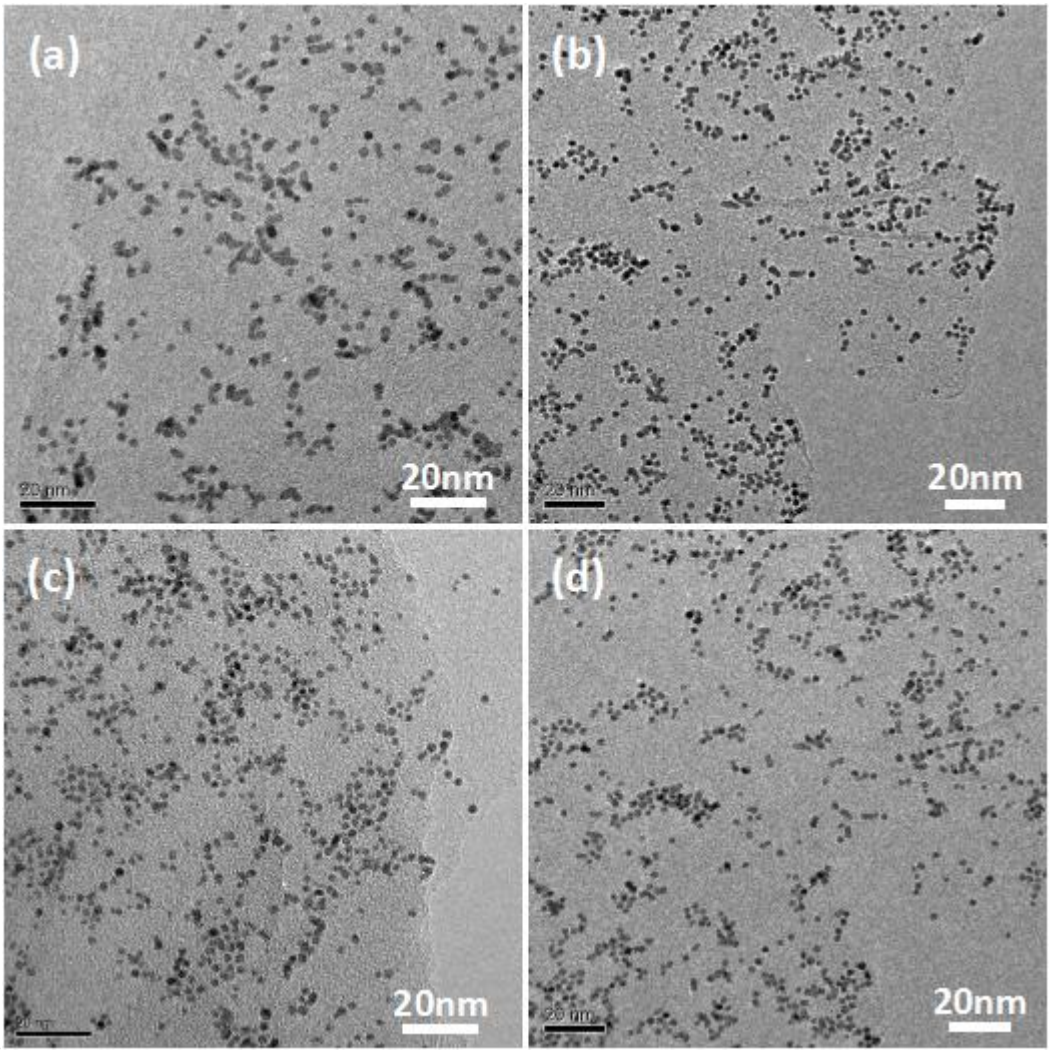

Figure 6. TEM images of fresh Pt/Gr. (a) Pt/Gr-200, (b) Pt/Gr-300, (c) Pt/Gr-400, (d) Pt/Gr-500. Different amount of micropores and oxygen active sites of Gr result in various Pt loading and dispersing.

Fig. 6. exhibits the TEM images of Pt/Gr nanocomposites. The homogeneous distribution of Pt nanoparticles on filmy Gr surface and no particles can be observe out of the supports, suggesting a strong interaction force between the graphene supports and Pt particles. Highly dispersed Pt nanoparticles on supports have advantage in catalytic activity, which is associated with the micropores and the active sites of oxygen containing functional groups of Gr, simultaneously [29]. With the increase in temperature for thermal treatment, the number of micropores increased but the oxygen content reduced. Thus there is an equilibrium point for the best dispersion of Pt nanoparticles. Fig. 6a shows an accumulation of partial Pt nanoparticles because of the less micropores and larger active sites. Fig. 6d presents a narrow size of Pt nanoparticles but with sparse distribution, which on account of the efficient exfoliation of oxygen containing functional groups. The representative TEM image of Pt/Gr-400 (Fig. 6c), compared to others, shows a better and homogeneous distribution of Pt nanoparticles on the ultrathin graphene sheets and owns higher catalytic activity. This is also in agreement with the X-ray diffraction patterns of the Pt/Gr catalysts in Fig. 2.

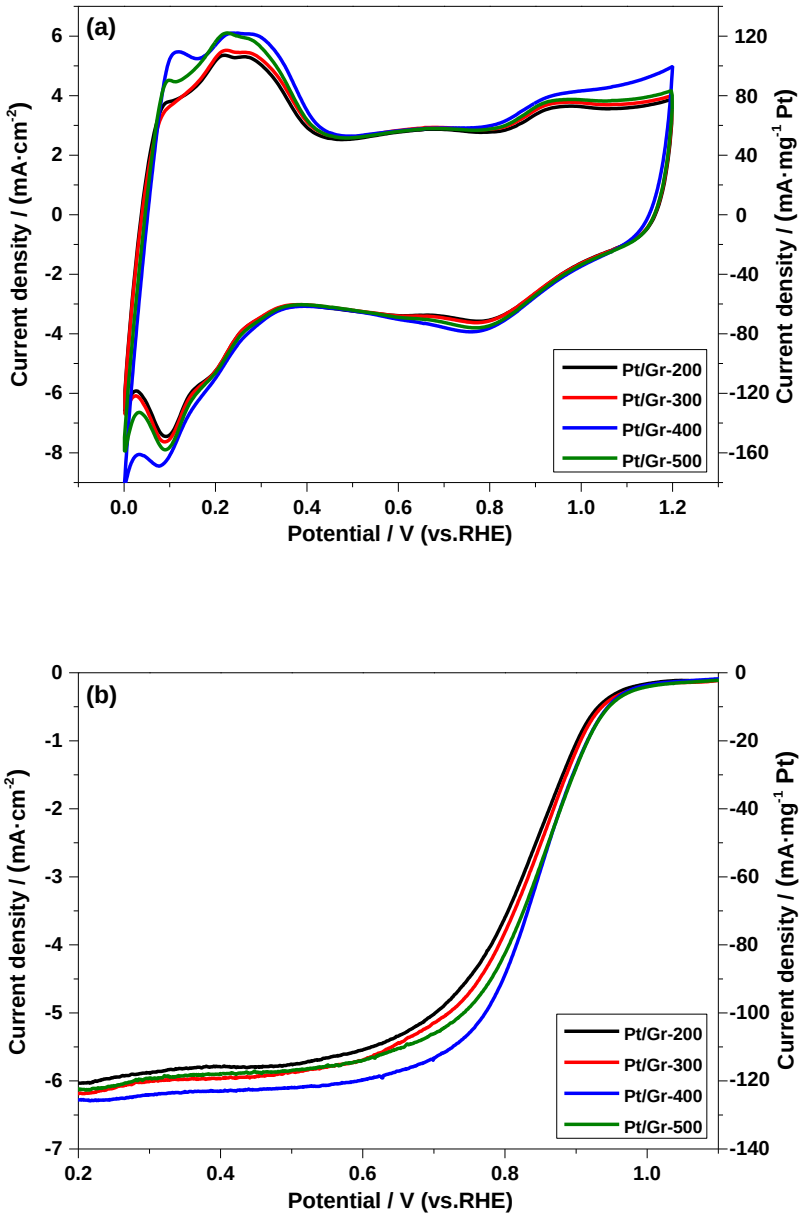

Figure 7. The cyclic voltammograms (CVs): (a) and the oxygen reduction linear sweep voltammetries (LSVs): (b) on fresh Pt/Gr electrodes; CVs were recorded in N_2-saturated 0.1 M $HClO_4$ (50 $mV \cdot s^{-1}$, room temperature) and LSVs were recorded in O_2-saturated 0.1 M $HClO_4$ (5 $mV \cdot s^{-1}$, 1600 rpm, room temperature).

Cyclic voltammograms (CVs) of Pt/Gr in $HClO_4$ solution with N_2-saturated are demonstrated in Fig. 7a. It is clearly seen that the Pt/Gr catalyst has a typical hydrogen and oxygen adsorption/ desorption behavior. Coulombic charges accumulated is used to calculate the electrochemical surface area (ESA) of platinum catalyst during hydrogen adsorption and desorption after correcting for the double-layer charging current from the CVs: $ESA = Q_H / (0.21 \cdot m_{Pt})$, where m_{Pt} is the mass of Pt loaded on the working electrode, 0.21 $mC \cdot cm^{-2}$ is the electrical charge associated with monolayer adsorption

of hydrogen on Pt, Q_H (mC) stands for the charge due to the hydrogen adsorption/ desorption in the hydrogen region (0.03-0.37 V) of the CVs [30]. It is informed that the ESA of Pt/Gr-400 in the initial cycle is 157.34 $m^2 \cdot g^{-1}$, which is much higher than that of Pt/Gr-200, Pt/Gr-300 or Pt/Gr-500. The higher catalytic activity of Pt/Gr-400 can be attributed to the wee and homogeneous dispersion of Pt nanoparticles on Gr surface. The ESA of 157.34 $m^2 \cdot g^{-1}$ is also 2-3 times higher than that of commercial Etek Pt/C (20% Pt on Vulcan XC-72 from Etek Company, New Jersey, USA) [18, 23, 31]. Fig. 7b indicates the oxygen reduction reaction (ORR) on Pt/Gr electrocatalyst by the rotating disk electrode measurements at the rotation speed of 1600 rpm. Using Koutecky-Levich equation, the ORR activity of the electrocatalyst can be evaluated with the kinetic ORR current at 0.9 V [8]. The higher ORR activity on Pt/Gr-400 is indicated by the higher onset potential (0.96 V, initial) of O_2 reduction and the higher half-wave potential (0.85 V, initial) [32]. The ORR activity at 0.90 V of Pt/Gr-400 catalyst is calculated to be 26.6 $mA \cdot mg^{-1}_{Pt}$, which is higher than that of commercial Etek Pt/C [18, 23]. Correspondingly, the specific activity is 1.38 $mA \cdot cm^{-2}$. This significantly increased ORR activity on Pt/Gr-400 is most likely due to the higher electrochemical surface area of Pt nanoparticles on Gr, which results in high electrical conductivity [33, 34]. The relevant information of Pt/Gr-400 is listed in Table 2.

Table 2. Information of the fresh catalyst.

Electrode	Pt loading / ($g \cdot m^{-2}$)	ESA / ($m^2 \cdot g^{-1}$)	D(TEM) / nm	Onset potential/V	Have-wave potential/V
Pt/Gr-200	0.52	119.83	4.47	0.945	0.824
Pt/Gr-300	0.52	123.87	3.12	0.952	0.833
Pt/Gr-400	0.52	157.34	2.34	0.961	0.850
Pt/Gr-500	0.52	136.76	2.31	0.958	0.845

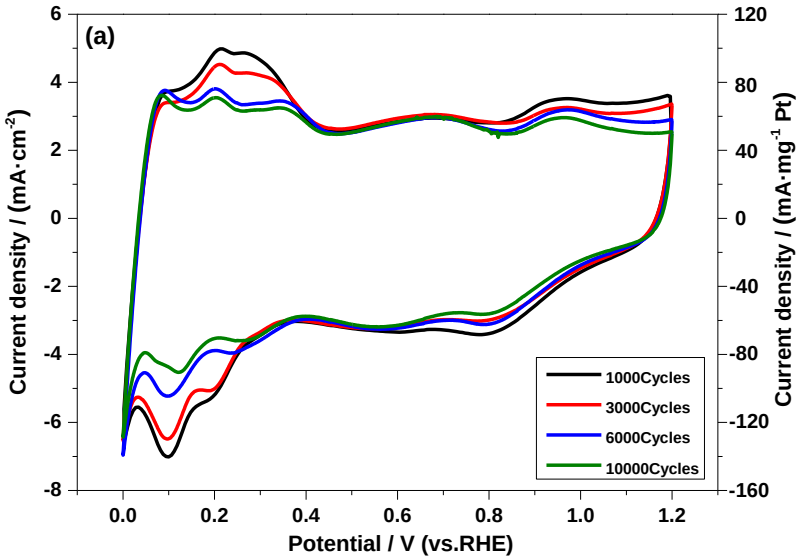

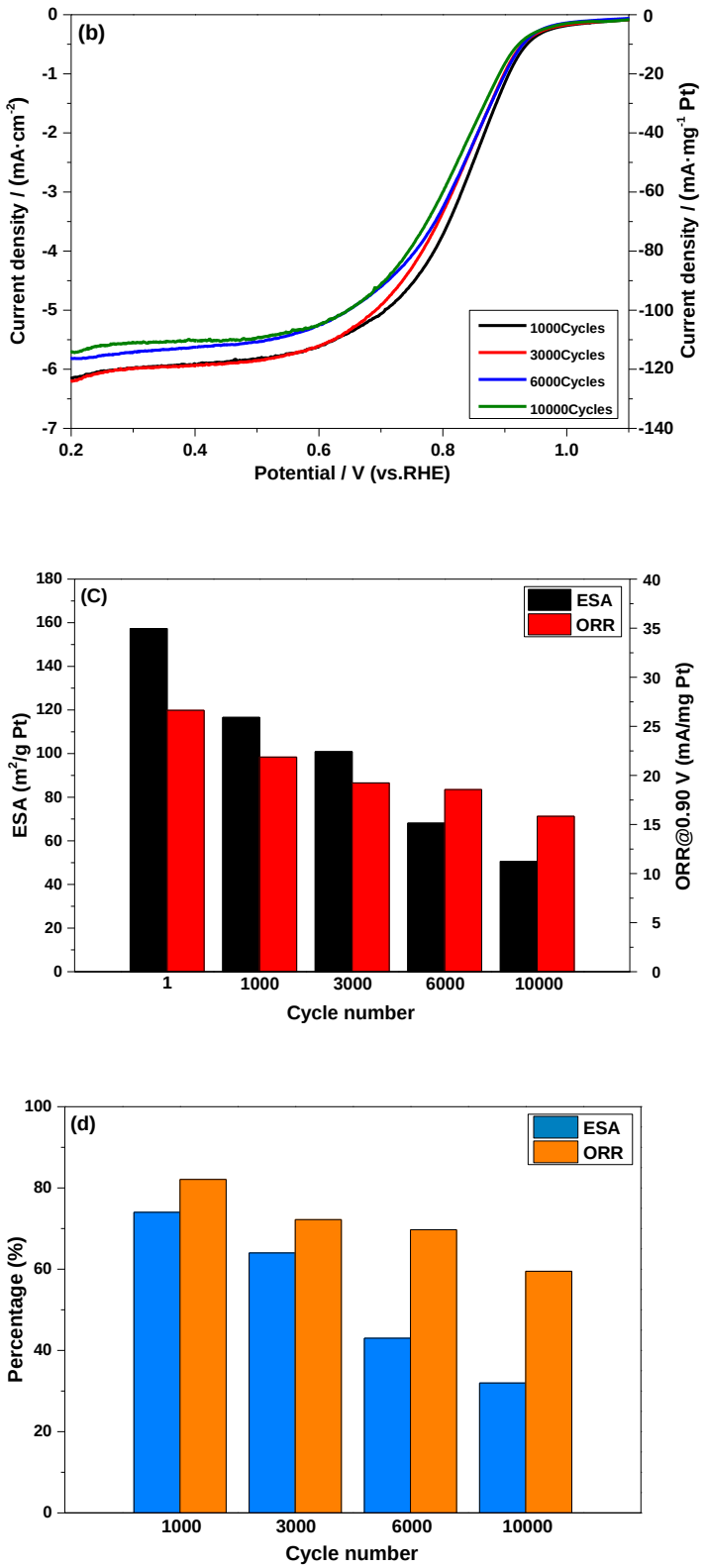

Figure 8. Electrochemical properties of Pt/Gr-400 after the durability test under potential steps of 0-1.2 V for 10000 cycles in 0.1 M $HClO_4$ aqueous solution. (a) Cyclic voltammograms under a scan rate of 50 $mV \cdot s^{-1}$; (b) polarization curves for the O_2 reduction (5 $mV \cdot s^{-1}$, 1600 rpm); (c) original values of ESA and ORR activity at 0.90 V; (d) the percentage of retaining ESA and ORR activity after degradation.

The long-term stability of Pt electrocatalyst is of great importance for the development of commercial PEMFCs [35]. Fig. 8 shows the changes in ESA and ORR activity of Pt/Gr-400 after the durability test under the potential step condition of 0-1.2 V for 10000 cycles [30]. After 10000 cycles, the ESA is still 50.63 $m^2 \cdot g^{-1}_{Pt}$ which is higher than 30 $m^2 \cdot g^{-1}_{Pt}$ of EtekPt/C after 5000 cycles. The ORR current density at 0.9 V is 15.84 $mA \cdot mg^{-1}_{Pt}$ (higher than 10.42 $mA \cdot mg^{-1}_{Pt}$ of EtekPt/C after 5000 cycles). The onset potential and the half-wave potential of ORR activity are also evaluated. After 10000 cycles, the onset potential is 0.942 V (98% retention) and the half-wave potential is 0.811 V (96% retention). The results demonstrate that Pt/Gr has higher durability in terms of both ESA and ORR activity than that of commercial EtekPt/C [16, 31].

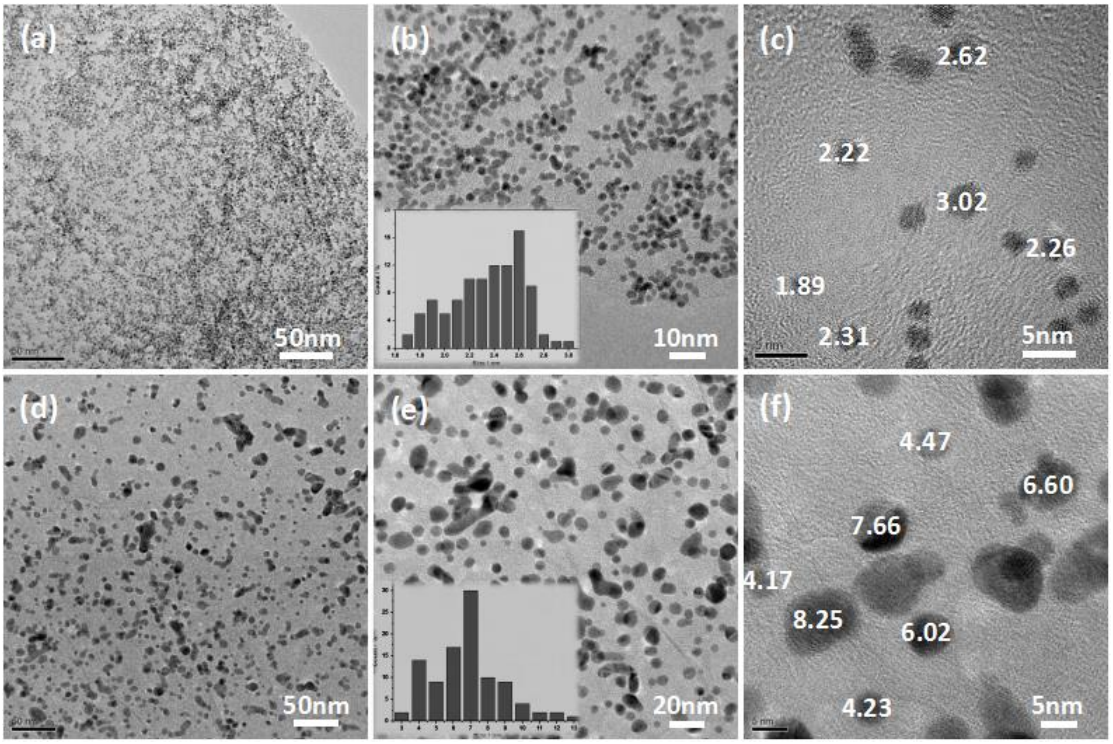

Figure 9. TEM images of Pt/Gr-400 before (a, b, c) and after (d, e, f) degradation of 10000 cycles, and size distribution diagrams of Pt nanoparticles (fresh inside b and aged inside e).

In addition, Fig. 9 shows TEM images of fresh and aged catalyst. Morphology of Pt did change and the effect of the supports on the morphological stability was studied. After 10000 cycles, the mean particle size of Pt in graphene-supported catalyst increased from 2.34 to 6.43 nm and over 72% of the Pt particles remained smaller than 7.0 nm. So the aggregation of Pt particles were directly result in the loss of the ESA and ORR activity. Due to the π sites and functional groups in graphene sheets, the durability was greatly enhanced by a strong metal-support interaction and resultant resistance of Pt to sintering [36, 37].

4. CONCLUSION

In summary, we report a facile method for the rapid and massive synthesis of high-quality graphene, which was employed as an alternative support material for oxygen reduction. The durability

and activity of Pt/Gr catalyst towards oxygen reduction reaction is determined by both the micropores and graphitization degree of graphene supports. The activity of Pt/Gr-400 is comparable to or even better than commercial Pt/C catalyst with the greatly enhanced durability. These are attributed to the highly dispersed micropores and considerable graphitization degree of Gr which enhanced Pt-carbon interaction in Pt/Gr. Being easily mass produced from natural graphite, graphene is low-cost and durable electrocatalyst support for oxygen reduction in fuel cells.

References

1. J. Zhang, K. Sasaki, E. Sutter, R. Adzic, *Science,* 315 (2007) 220.
2. C.J. Zhong, J. Luo, P. N. Njoki, D. Mott, B. Wanjala, R. Loukrakpam, S. Lim, L. Wang, B. Fang, Z. Xu, *Energy Environ. Sci.,* 1 (2008) 454.
3. L. Roen, C. Paik, T. Jarvi, *Electrochem. Solid-State Lett.,* 7 (2004) A19.
4. K. Lee, J. Zhang, H. Wang, D. P. Wilkinson, *J. Appl. Electrochem.,* 36 (2006) 507.
5. X. Wang, W. Li, Z. Chen, M. Waje, Y. Yan, *J. Power Sources,* 158 (2006) 154.
6. Y. Shao, S. Zhang, R. Kou, X. Wang, C. Wang, S. Dai, V. Viswanathan, J. Liu, Y. Wang, Y. Lin, *J. Power Sources,* 195 (2010) 1805.
7. J. Shim, C.R. Lee, H.K. Lee, J.S. Lee, E.J. Cairns, *J. Power Sources,* 102 (2001) 172.
8. H. A. Gasteiger, S. S. Kocha, B. Sompalli, F. T. Wagner, *Appl. Catal. B- Environ.,* 56 (2005) 9.
9. J. Tian, G. Sun, M. Cai, Q. Mao, Q. Xin, *J. Electrochem. Soc.,* 155 (2008) B187.
10. S. Sharma, B. G. Pollet, *J. Power Sources,* 208 (2012) 96.
11. S. Dou, L. Tao, J. Huo, S. Y. Wang, L. M. Dai, *Energy Environ. Sci.,* 9 (2016) 1320.
12. L. Tao, Q. Wang, S. Dou, Z. L. Ma, J. Huo, S. Y. Wang, L. M. Dai, *Chem. Commun.,* 52 (2016) 2764.
13. H. K. Chae, D. Y. Siberio-Pérez, J. Kim, Y. Go, M. Eddaoudi, A. J. Matzger, M. O'Keeffe, O. M. Yaghi, *Nature,* 427 (2004) 523.
14. K. Novoselov, A. K. Geim, S. Morozov, D. Jiang, M. Katsnelson, I. Grigorieva, S. Dubonos, A. Firsov, *Nature,* 438 (2005) 197.
15. Y. Hernandez, V. Nicolosi, M. Lotya, F. M. Blighe, Z. Sun, S. De, I. McGovern, B. Holland, M. Byrne, Y. K. Gun'Ko, *Nature Nanotech.,* 3 (2008) 563.
16. R. Kou, Y. Shao, D. Wang, M. H. Engelhard, J. H. Kwak, J. Wang, V. V. Viswanathan, C. Wang, Y. Lin, Y. Wang, *Electrochem. Commun.,* 11 (2009) 954.
17. Y. Li, L. Tang, J. Li, *Electrochem. Commun.,* 11 (2009) 846.
18. Y. Shao, S. Zhang, C. Wang, Z. Nie, J. Liu, Y. Wang, Y. Lin, *J. Power Sources,* 195 (2010) 4600.
19. S.Y. Yang, K.H. Chang, Y.F. Lee, C.C. M. Ma, C.C. Hu, *Electrochem. Commun.,* 12 (2010) 1206.
20. X. Zhou, J. Qiao, L. Yang, J. Zhang, *Adv. Energy Mater.,* 4 (2014).
21. W. S. Hummers Jr, R. E. Offeman, *J. Am. Chem. Soc.,* 80 (1958) 1339.
22. X. Huang, X. Qi, F. Boey, H. Zhang, *Chem. Soc. Rev.,* 41 (2012) 666.
23. S. Zhang, Y. Shao, X. Li, Z. Nie, Y. Wang, J. Liu, G. Yin, Y. Lin, *J. Power Sources,* 195 (2010) 457.
24. Y. Shao, R. Kou, J. Wang, V. V. Viswanathan, J. H. Kwak, J. Liu, Y. Wang, Y. Lin, *J. Power Sources,* 185 (2008) 280.
25. Z.S. Wu, Y. Sun, Y.Z. Tan, S. Yang, X. Feng, K. Müllen, *J. Am. Chem. Soc.,* 134 (2012) 19532.
26. W. Chen, L. Yan, *Nanoscale,* 2 (2010) 559.
27. J. I. Paredes, S. Villar-Rodil, P. Solís-Fernández, A. Martínez-Alonso, J. Tascon, *Langmuir,* 25 (2009) 5957.

28. A. Kaniyoor, T. T. Baby, S. Ramaprabhu, *J. Mater. Chem.*, 20 (2010) 8467.
29. F. Zhang, Z. Wang, Y. Zhang, Z. Zheng, C. Wang, Y. Du, W. Ye, *Int. J. Electrochem. Sci.*, 7 (2012) 1968.
30. S. Zhang, Y. Shao, G. Yin, Y. Lin, *Appl. Catal. B- Environ.*, 102 (2011) 372.
31. J. Wang, G. Yin, Y. Shao, S. Zhang, Z. Wang, Y. Gao, *J. Power Sources*, 171 (2007) 331.
32. K. Sasaki, L. Zhang, R. Adzic, *PCCP*, 10 (2008) 159.
33. W. Li, C. Liang, W. Zhou, J. Qiu, Z. Zhou, G. Sun, Q. Xin, *J. Phys. Chem. B*, 107 (2003) 6292.
34. A. Kongkanand, K. Vinodgopal, S. Kuwabata, P. V. Kamat, *J. Phys. Chem. B*, 110 (2006) 16185.
35. R. Borup, J. Meyers, B. Pivovar, Y. S. Kim, R. Mukundan, N. Garland, D. Myers, M. Wilson, F. Garzon, D. Wood, *Chem. Rev.*, 107 (2007) 3904.
36. F. Coloma, A. Sepulvedaescribano, F. Rodriguezreinoso, *J. Catal.*, 154 (1995) 299.
37. D. Stevens, M. Hicks, G. Haugen, J. Dahn, *J. Electrochem. Soc.*, 152 (2005) A2309.